JOURNAL OF SPACECRAFT AND ROCKETS
Vol. 36, No. 5, September–October 1999

# Transition Effects on Heating in the Wake of a Blunt Body

Brian R. Hollis*
*NASA Langley Research Center, Hampton, Virginia 23681-2199*
and
John N. Perkins†
*North Carolina State University, Raleigh, North Carolina 27695-7910*

**A series of aerodynamic heating tests was conducted on a 70-deg sphere-cone planetary entry vehicle model in a Mach 10 perfect-gas wind tunnel at freestream Reynolds numbers based on model diameter of $8.23 \times 10^4$ to $3.15 \times 10^5$. Surface heating distributions were determined from temperature time histories measured on the model and on its support sting using thin-film resistance gauges. The experimental heating data were compared to computations performed using an axisymmetric/two-dimensional, laminar, perfect-gas Navier–Stokes solver. On the forebody of the vehicle, as well as on the sting upstream of the free-shear-layer reattachment point, comparisons between the measured and computed heating distributions were within, or slightly greater than, the estimated uncertainty of the experimental data. However, the comparisons diverged after the reattachment point, with the experimental data becoming increasingly greater than the computations with distance downstream from the reattachment point. It was theorized that this disagreement was because of the transition of the wake free shear layer just upstream of the reattachment point on the sting.**

## Nomenclature

$C_H$ = Stanton number, $q/[\rho_1 u_1 (h_0 - h_w)]$
$d$ = molecular diameter, m
$h$ = enthalpy, J/kg
$Kn$ = Knudsen number, $\lambda|\nabla\rho|/\rho$
$M$ = Mach number
$N$ = number density, $1/m^3$
$p$ = pressure, $N/m^2$
$q$ = heat transfer rate, $W/m^2$
$R$ = radius, m
$Re$ = Reynolds number
$S$ = distance along model surface, m
$T$ = temperature, K
$t$ = time, s
$U_1$ = freestream velocity, m/s
$\lambda_{mfp}$ = mean free path, m $= 1/[\sqrt{2}(\pi d^2 N)]$
$\rho$ = density, $kg/m^3$

*Subscripts*

$D$ = diameter
$w$ = wall
0 = stagnation
1 = freestream
2 = postshock

## Introduction

WAKE-FLOW behavior is one of the important issues that must be considered in the design of planetary entry vehicles such as the Mars Pathfinder probe[1] because it influences payload size, placement, and shielding requirements. Accurate characterization of the wake-flow behavior is becoming more important because of the increasing reliance in planetary mission planning on aerobraking, which produces much more severe aerothermodynamic loads on an entry vehicle.

In this study the effects of transition in the wake of a blunt body were investigated through heat-transfer testing of a 70-deg sphere-cone entry vehicle configuration in a perfect-gas hypersonic wind tunnel. Other recent studies[2–15] also have addressed the effects of nonequilibrium thermochemistry, rarefaction, and transition to turbulence on wake-flow behavior.

## Experiment Description

### Test Models

The test-model geometry was a 70-deg sphere-cone forebody of 1.0-in. radius with a 40-deg cone-frustrum afterbody (Fig. 1). The forebody corner radius was 0.05 forebody radii, and the radius of the hemispherical nose was 0.5 forebody radii. The afterbody frustrum radius was 0.6 forebody radii.

A heat-transfer test model was fabricated from MACOR®, a thermally-insulative, machinable glass-ceramic material (Fig. 2). The model was instrumented with fast-response (<1 $\mu$s) thin-film temperature resistance gauges. There were a total of 37 gauges on the forebody, afterbody, and base of the model. The support sting for this model was fabricated from stainless steel, and a contoured MACOR insert with 33 additional thin-film gauges was fitted into it. The support sting was mated to a sting adapter and the facility support barrel at a distance of 5.25 forebody radii downstream of the model. An additional uninstrumented model and sting were fabricated from aluminum for use in oil-flow tests.

### Facility Description

Aerothermodynamic testing was conducted in the NASA Langley Research Center 31-Inch Mach 10 Air Tunnel.[16] This facility is a conventional, perfect-gas, hypersonic blowdown wind tunnel and has been calibrated for operation at reservoir pressures of 0.86–10 MPa at a reservoir temperature of 1000 K. These reservoir conditions produce freestream Reynolds numbers from $1.62 \times 10^6$ $m^{-1}$ to $6.20 \times 10^6$ $m^{-1}$ at a nominal freestream Mach number of 10. Although longer run times are possible for aerodynamic testing, facility run times for the current series of heat-transfer tests were limited to 3–5 s to avoid violation of the semi-infinite heat transfer assumption[17] and to minimize the effects of increasing surface temperatures on the heat-transfer distributions. Freestream conditions for this study are listed in Table 1. The run-to-run repeatability of these conditions was investigated and was found to be within less than ±2%.

Received 1 August 1997; revision received 15 November 1998; accepted for publication 15 December 1998. 

*Aerospace Engineer, Aerothermodynamics Branch. Member AIAA.
†Professor, Department of Mechanical and Aerospace Engineering. Associate Fellow AIAA.

### Experimental Results

The 70-deg sphere-cone heat-transfer model was tested in the 31-Inch Mach 10 Air Tunnel at freestream Reynolds numbers based on model diameter of $8.23 \times 10^4$, $1.62 \times 10^5$, and $3.15 \times 10^5$. Reduction and analysis of the thin-film gauge data from these tests were accomplished following the procedures described in Ref. 2. The experimental results are reported in terms of the Stanton number, which remains nominally constant during a test, as opposed to the heat-transfer rate, which decreases during a test as the wall-surface temperature and enthalpy increases. Again following the procedure described in Ref. 2, estimates of ±7–8% were made for the experimental uncertainty of the data.

Stanton-number distributions normalized by the measured stagnation point values from tests at each of the three Reynolds numbers are plotted in Fig. 3a for the forebody and Fig. 3b for the wake. The Reynolds number had no effect on the normalized forebody heating distribution, but did have a strong influence on the heating distribution in the wake where the normalized heating was an increasing function of the Reynolds number. The peak heating on the model sting varied from 8% of the forebody stagnation point heating at the lowest Reynolds number to 15% at the highest Reynolds number. Relative peak sting heating rates of this level are consistent with turbulent wakes,[6,7,14] whereas relative laminar peak sting heating levels are in the 4–5% range.[12–15]

Several surface oil-flow tests also were performed using the uninstrumented aluminum model. On the inspection of the oil-flow photographs from these tests, identifying the boundary-layer separation point on the afterbody and the free shear-layer reattachment point on the sting was possible. A sample surface oil-flow photograph is shown in Fig. 4. The reattachment point on the sting moved a small distance upstream toward the model as the Reynolds number was increased. This behavior is typical of increasing turbulence in the free shear layer: as the turbulence increases, momentum dissipation causes its thickness to increase, and the thicker turbulent free shear layer then comes into contact with the sting further upstream than a laminar free shear layer would.

**Table 1 31-Inch Mach 10 Air Tunnel test conditions**

| Parameter | $Re_{1,D} = 8.23 \times 10^4$ | $Re_{1,D} = 1.62 \times 10^5$ | $Re_{1,D} = 3.15 \times 10^5$ |
|---|---|---|---|
| $P_1$, Pa | 69.0 | 130.6 | 242.0 |
| $T_1$, K | 53.31 | 52.45 | 51.48 |
| $\rho_1$, kg/m$^3$ | 0.00451 | 0.00868 | 0.01646 |
| $U_1$, m/s | 1,416 | 1,422 | 1,425 |
| $M_1$ | 9.675 | 9.795 | 9.928 |
| $h_0 - h_{298K}$, MJ/kg | 0.756 | 0.764 | 0.767 |
| $p_{0,2}$, Pa | 8,383 | 16,280 | 31,000 |
| $T_{0,2}$, K | 1,008 | 1,015 | 1,017 |

## Computations

### Code Description

Flowfield solutions for the 70-deg sphere-cone geometry were generated using the laminar, axisymmetric/two-dimensional Navier–Stokes solver NEQ2D.[18] A perfect-gas thermochemical model was used to reproduce conditions equivalent to those of the 31-Inch Mach 10 Air Tunnel tests, although NEQ2D also does incorporate nonequilibrium thermochemical models. The governing equations are solved in NEQ2D through the line Gauss–Seidel method. Inviscid fluxes are represented by a modified form[19] of the Beam–Warming flux-splitting technique that minimizes the numerical dissipation produced in boundary layers by the original form. Viscous fluxes are represented by second-order central differences.

### Grid Generation, Adaption, and Resolution

An initial grid of 125 streamwise by 90 normal points for the sphere-cone geometry was created using an elliptical grid generation algorithm.[20] Orthogonality and initial cell spacing at the wall were enforced through Steger–Sorenson[21] boundary conditions. During computation of a solution, the grid was aligned with the bow shock, and cells were clustered at the wall using an algebraic grid-adaption algorithm.[22]

The wake computations were found to be extremely sensitive to the structure of the wake grid. This sensitivity is because the wake free shear layer and recirculation vortex are viscous-dominated regions. To properly resolve the flowfield gradients in these regions, grid resolution in the wake vortex and free shear layer must be of the same order as found in attached wall boundary layers.

To optimize the wake-grid structure, the Volume Grid Manipulator[23] (VGM) code was used to cluster grid points within the recirculation vortex and to align the streamwise grid lines with the

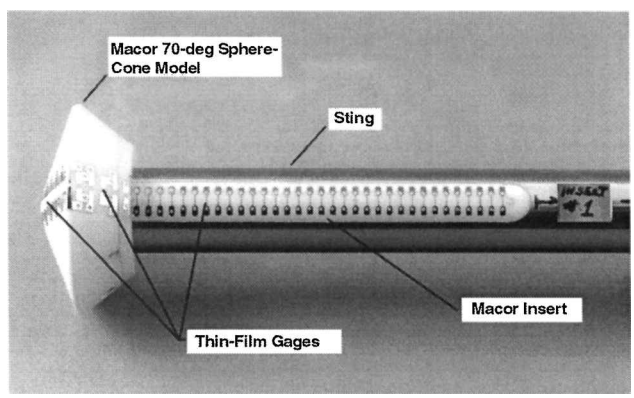


**Fig. 2 Entry vehicle model photograph.**

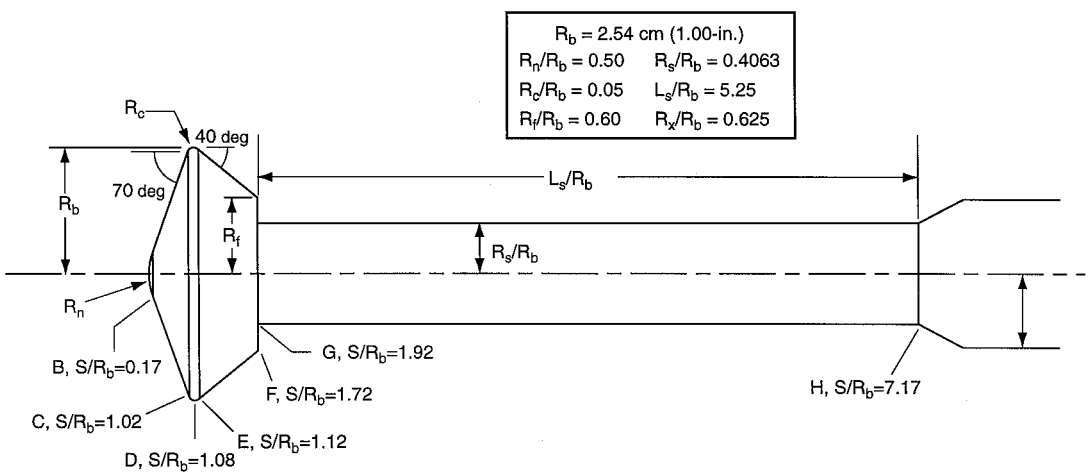


**Fig. 1 Entry vehicle model geometry.**

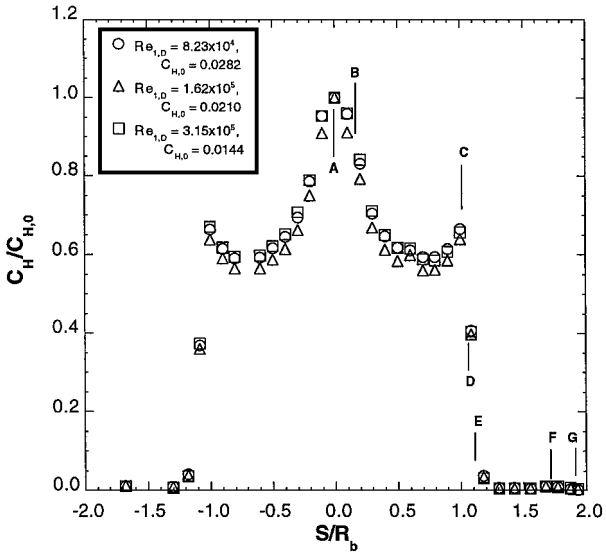


**Fig. 3a Reynolds number effects on experimental forebody heating.**

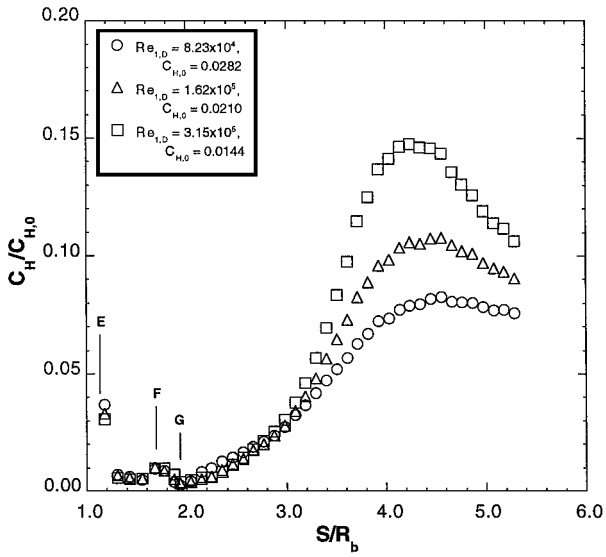


**Fig. 3b Reynolds number effects on experimental wake heating.**

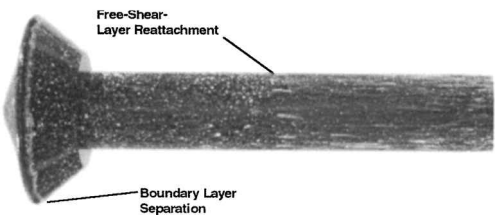


**Fig. 4 Sample oil-flow patterns.**

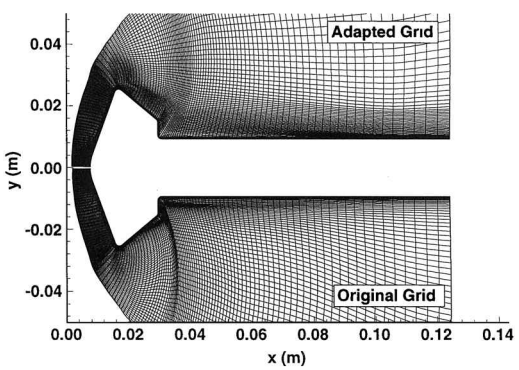


**Fig. 5 Comparison of adapted and nonadapted grids.**

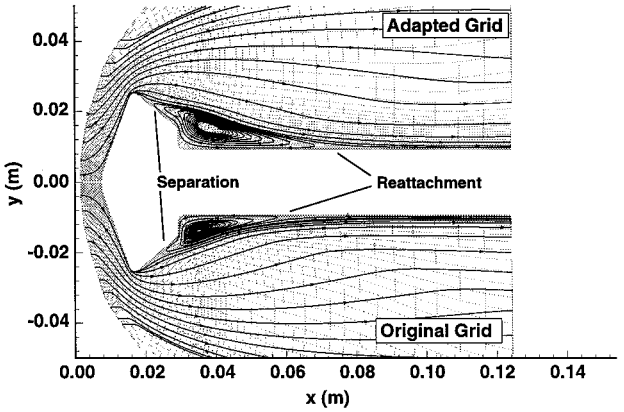


**Fig. 6 Effects of grid adaption on wake flow.**

free shear layer (Fig. 5) after an initial flowfield solution was computed. This adaption produced significant changes in the structure of the wake flowfield. As seen in Fig. 6, the free-shear-layer reattachment point on the wake-adapted grid moved downstream from the computed location on the unadapted grid, thus increasing the size of the recirculation vortex. This growth is because the numerical dissipation produced by the lack of resolution within the wake vortex is minimized by the adaption of the wake grid.

In addition to the effects of the wake-grid structure on the computed solutions, the effects of grid density also were investigated. Flowfield solutions were found to be relatively insensitive to streamwise grid resolution as compared to the sensitivity to normal grid resolution. Therefore, to investigate the effects of normal grid resolution on the solution, grids with 125 streamwise points and 45, 179, and 357 normal points were created from the baseline ($125 \times 90$) point shear-layer-adapted grid.

The forebody computations (Fig. 7a) were relatively insensitive to normal grid-point resolution. The greatest sensitivity was observed around the nose and corner heating peaks where the heating rates decreased by less than 5% between the 45 and 90 normal points grids and by ~1% between the 90 and 179 point grids.

Wake computations (Fig. 7b) were much more sensitive to grid resolution than forebody computations, as would be expected given the much larger viscous region to be resolved in the wake. The sensitivity was greatest on the area of the sting bounded by the recirculation vortex, whereas the computations on the portions of the afterbody and sting over which the flow was attached showed less sensitivity. On the region of the sting within the wake vortex, heating rates decreased by more than 10% between the 45 and 90 normal point grids, by 5–10% between the 90 and 179 point grids, and by less than 5% between the 179 and 357 point grids.

From this grid-resolution study the conclusion was made that 90 normal points were more than sufficient to model the forebody flow and the attached flow on the afterbody and on the sting downstream of the vortex. However, within the recirculation vortex, acceptable results were achieved only on the highest resolution, 357 normal point grid.

### Computational Results

Solutions were computed for each of the three Reynolds numbers on free-shear-layer-adapted ($125 \times 357$) point grids using the NEQ2D code. Freestream flow conditions were taken from Table 1, and a uniform 300 K wall temperature was specified. These computations revealed complex recirculating flow patterns in the near wake of the body. As shown in Fig. 8, a large primary vortex was generated between the free shear layer and body, and smaller counter-rotating vortices were formed at the base of the vehicle and on the afterbody. The size of the main vortex increased with Reynolds number, which is the theoretically expected behavior in a laminar wake: as the Reynolds number is increased, more momentum is added to the shear layer, and thus the reattachment point is pushed further downstream from the separation point on the body. The size of the secondary vortices also depended on Reynolds number, and at the lowest Reynolds number the smaller afterbody vortex disappeared.

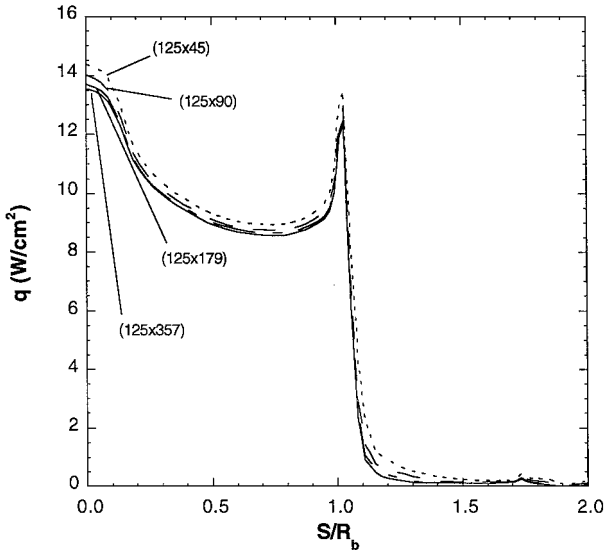


**Fig. 7a Grid-resolution effects on forebody computations for $Re_{1,D}$ = 8.23 × 10⁴ case.**

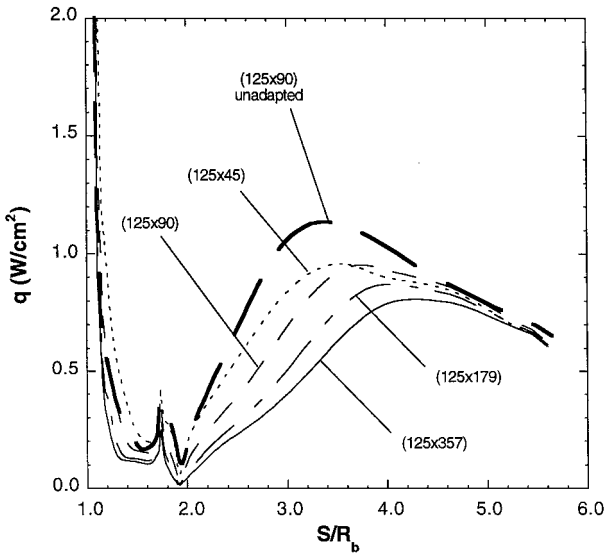


**Fig. 7b Grid-resolution effects on wake computations for $Re_{1,D}$ = 8.23 × 10⁴ case.**

Heat-transfer distributions normalized by the computed stagnation point values for each of the three Reynolds numbers are plotted in Fig. 9a for the forebody and Fig. 9b for the wake. As in the experiments, the Reynolds number had no effect on the normalized forebody heating distribution (the slight spread in the forebody distributions is attributed to the use of the same boundary-layer grid spacing for each of the three different Reynolds numbers), whereas in the wake, the normalized peak sting heating increased with Reynolds number.

## Comparison of Experiment and Computations

Measured and predicted heating distributions for each of the three Reynolds numbers are compared in Figs. 10–12. Dimensional values for the experimental data were extrapolated to the uniform 300 K wall temperature of the computations through the definition of the Stanton number. Uncertainty bounds shown in these figures correspond to the ±7–8% estimate for experimental uncertainty.

Agreement between the data sets was very good on the forebody for all test cases. Computed heating rates were consistently higher than the experimental data, but remained within or just slightly outside of the estimated experimental uncertainty bounds.

In contrast to the forebody results, computational and experimental wake-heating distributions differed significantly. Fair agreement was achieved on the afterbody and on the sting near the base of the

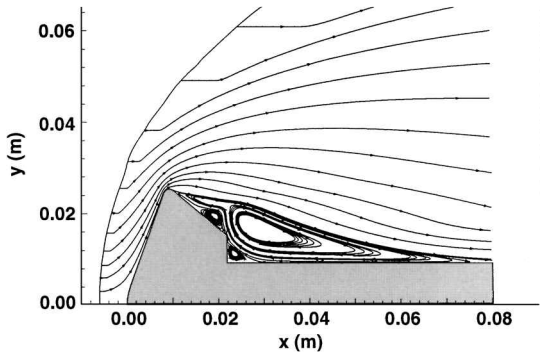


**Fig. 8 Sample computed wake streamlines.**

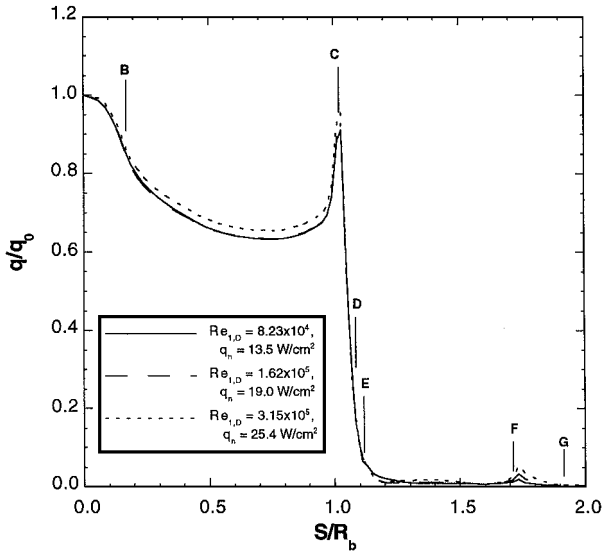


**Fig. 9a Reynolds number effects on computed forebody heating.**

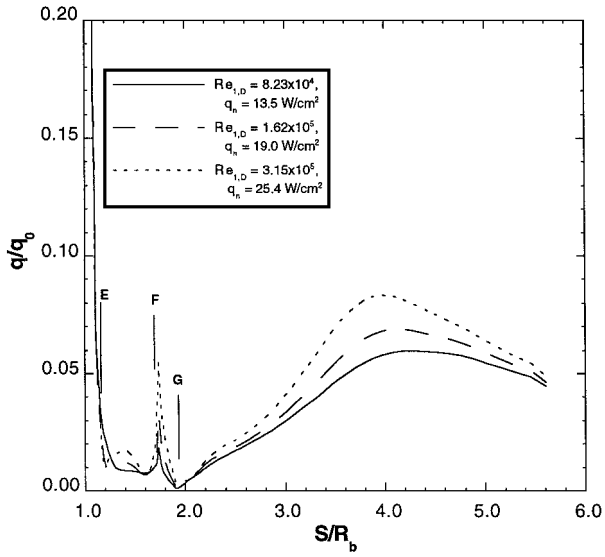


**Fig. 9b Reynolds number effects on computed wake heating.**

model; however, the two distributions begin to diverge just upstream of the free-shear-layer reattachment point on the sting. Furthermore, whereas computed peak sting heating rates only varied with the Reynolds number from 6 to 8% of the stagnation point rate, the experimental values ranged from 8 to 15% of the stagnation point rate. It was theorized that the divergence of the experimental and computational results was because of the growth of turbulence in the reattached boundary layer on the sting and that transition occurred

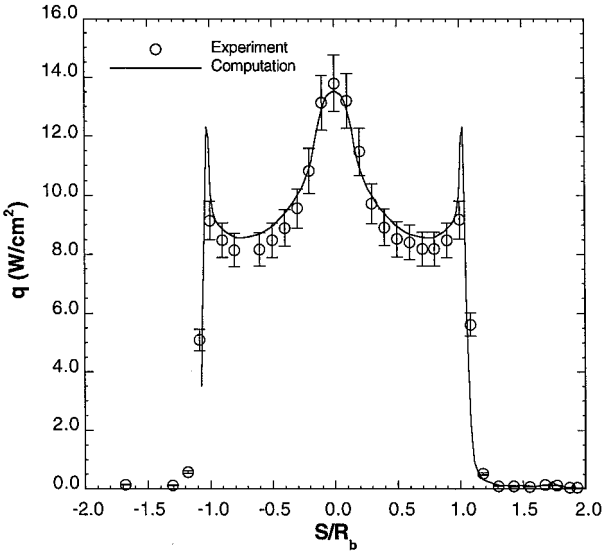


Fig. 10a Forebody-heating comparison at $Re_{1,D} = 8.23 \times 10^4$.

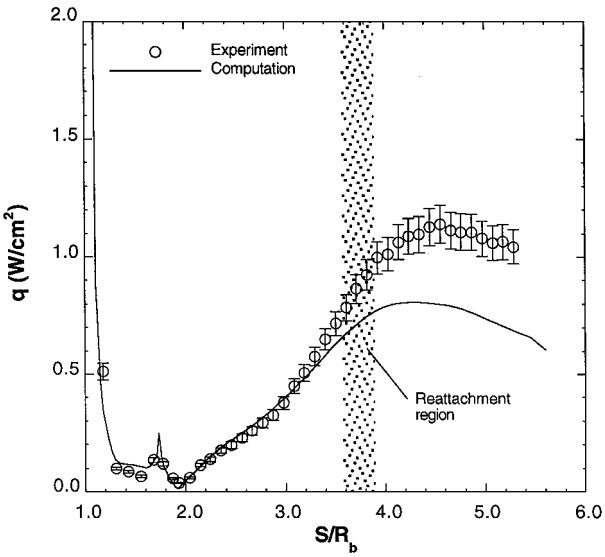


Fig. 10b Wake-heating comparison at $Re_{1,D} = 8.23 \times 10^4$.

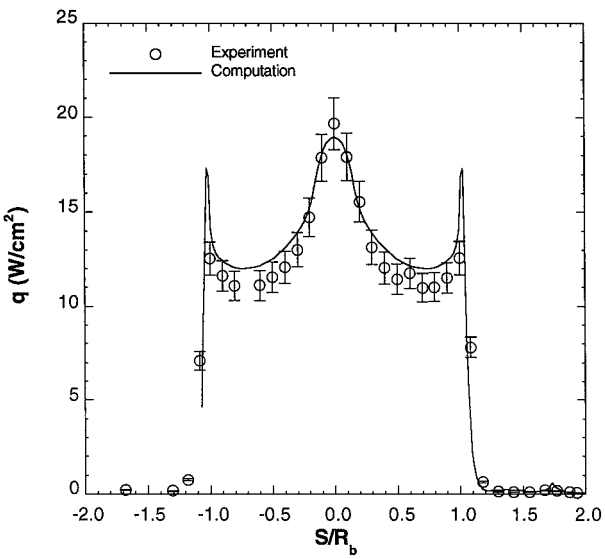


Fig. 11a Forebody-heating comparison at $Re_{1,D} = 1.62 \times 10^5$.

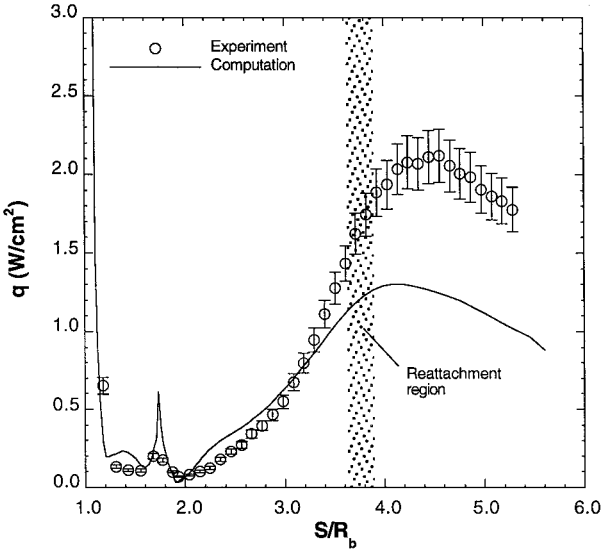


Fig. 11b Wake-heating comparison at $Re_{1,D} = 1.62 \times 10^5$.

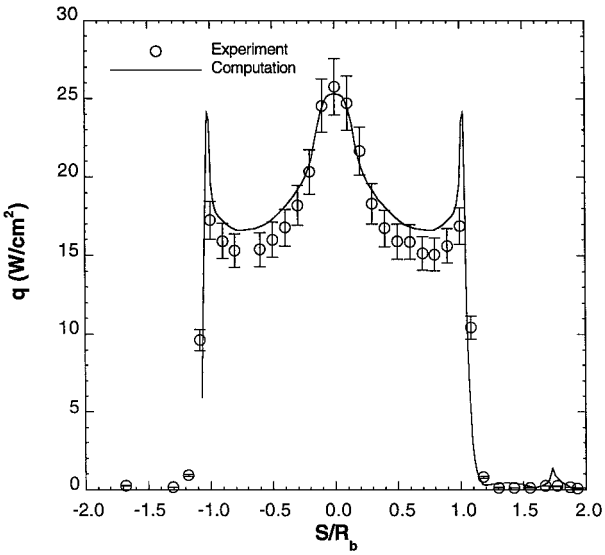


Fig. 12a Forebody-heating comparison at $Re_{1,D} = 3.15 \times 10^5$.

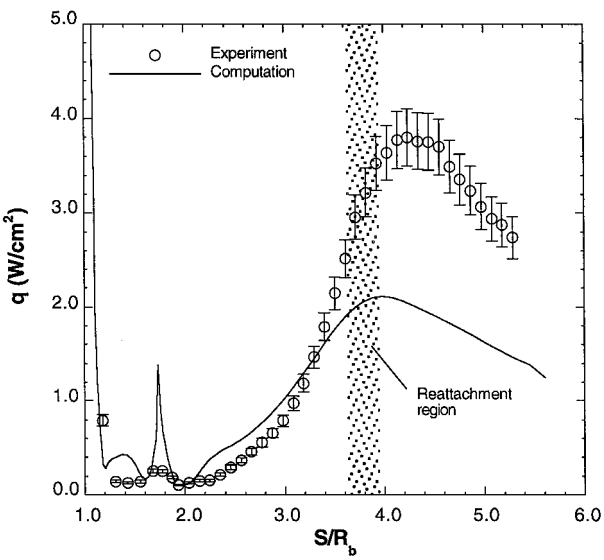


Fig. 12b Wake-heating comparison at $Re_{1,D} = 3.15 \times 10^5$.

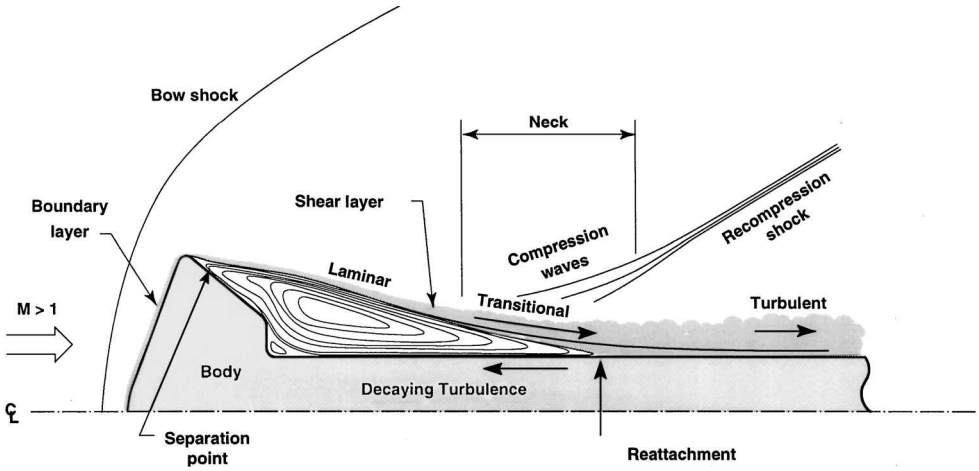


**Fig. 13 Transition in blunt-body wake free shear layer.**

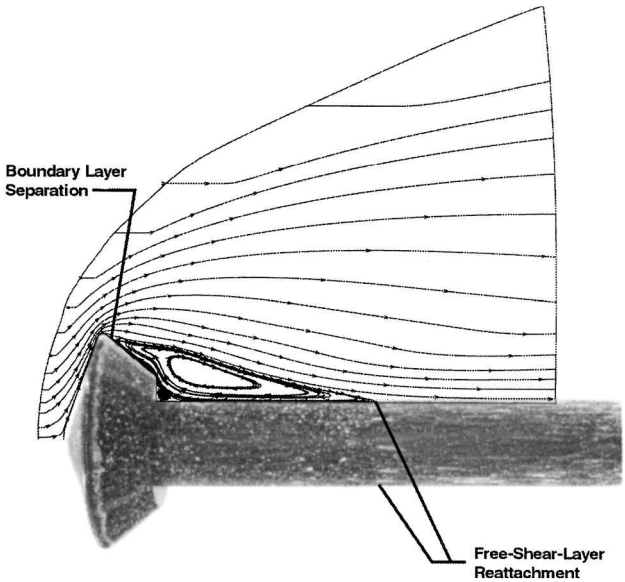


**Fig. 14 Comparison of oil-flow patterns and wake streamline computations.**

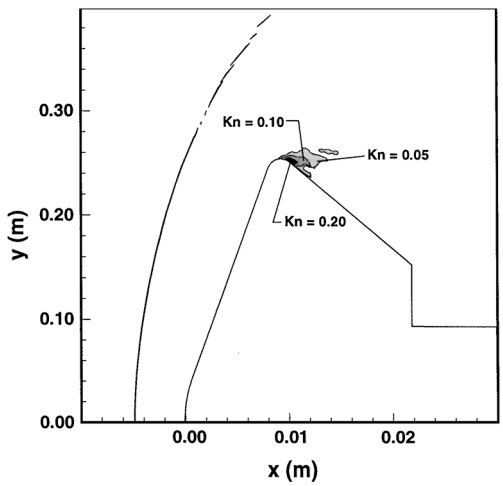


**Fig. 15 Local Knudsen number contours at $Re_{1,D} = 8.23 \times 10^4$.**

just upstream of the free-shear-layer reattachment point (Fig. 13), which is where the heating distributions begin to differ.

Although transition had a large effect on the flow downstream of reattachment, it had little effect on the flow within the wake vortex because the favorable pressure gradient produced as the reversed flow within the vortex accelerates from rest at the reattachment stagnation point tends to dissipate turbulence ingested into the wake vortex. For this reason the computed laminar heating distributions upstream of reattachment and the computed vortex sizes agree fairly well with the experimental data.

The theory that the reattachment region is where transition occurs is based on studies by Lees,[24] Demetriades,[25] and Zeiberg.[26] In these studies at low Reynolds numbers transition first occurs far downstream from the reattachment point (or from the neck of the wake in the case of an actual vehicle, which would not have a sting and reattachment point). As the Reynolds number is increased, the transition point moves upstream until it reaches the reattachment point (or neck). Because of the increasing pressure gradient that is caused as the flow is decelerated and turned at reattachment, the reattachment region acts as a trigger for transition, and so the transition point remains fixed here across a wide range of Reynolds numbers. Eventually, the Reynolds number is high enough for transition to occur in the free shear layer, and the transition point begins to move upstream within the free shear layer.

Comparisons between the computed streamlines and the oil-flow photographs support the hypothesis that transition occurs near the reattachment point. Although the laminar computations predict a small downstream movement of the separation point with Reynolds number while the oil-flow photographs suggest a small upstream movement, the actual locations were close (Fig. 14), which suggests that transition cannot be occurring very far upstream of reattachment. Furthermore, the computed and observed locations of the boundary-layer separation on the afterbody of the model are also close, which would suggest that the attached boundary layer on the model is laminar, as does the good agreement between measured and predicted heating distributions on the forebody experiment.

The transition of the free shear layer to turbulent flow and the location of the transition point have been presented as hypotheses. Transition appears to be the best explanation for the discrepancies between predicted and measured heating levels on the sting, which are much greater than the estimated experimental uncertainty. However, without flowfield diagnostics such as hot-wire surveys, or schlieren or electron-beam photography, which were not available in this study, definitive conclusions about the state of the free shear layer cannot be made. Nevertheless, two other possible causes of disagreement between experiment and computation can be eliminated: computational grid structure and rarefaction effects in the wake.

Although it has been shown that the wake computations can be very sensitive to the grid structure, all grid adaptions and grid-resolution improvements performed in this work had the effect of lowering the heating on the sting and moving the reattachment point further downstream. That is, optimization of the wake grid further increased the differences between computational and experimental results. Therefore, the grid structure cannot be the cause of the differences between experiment and computation.

To confirm that the Navier–Stokes equations for continuum flow were applicable for the low-density flow in the wake of the model,

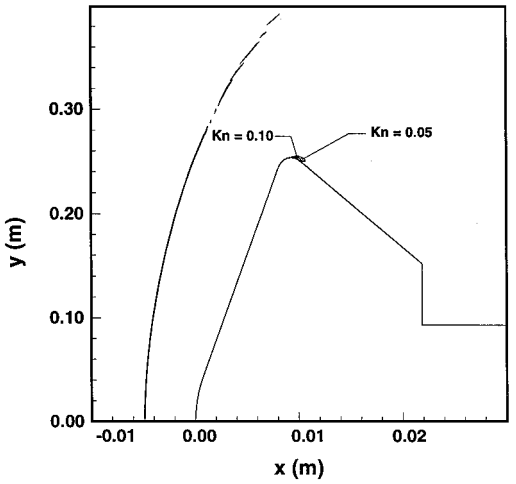


**Fig. 16 Local Knudsen number contours at $Re_{1,D} = 3.15 \times 10^5$.**

local Knudsen number contours were computed. According to Bird,[27] the continuum assumption begins to break down for local Knudsen numbers above 0.1, and for values above 0.2 the Navier–Stokes equations are no longer valid. Local Knudsen number contours for the highest- and lowest-Reynolds-number cases are shown in Figs. 15 and 16. For the high-Reynolds-number case, the local Knudsen numbers reach 0.1 only in a thin region near the separation point, whereas the local Knudsen number reaches the 0.2 level only in a small area around the separation point for the low-Reynolds-number case. Therefore, the Navier–Stokes equations are considered to be appropriate for the conditions of this study, and rarefaction effects cannot be the reason for the differences in the measured and predicted heating rates.

In regard to grid structure, it is also important to note that computations on grids of insufficient quality can suggest incorrect conclusions when comparisons are made with experimental results. As can be seen from the present results, the magnitude of a computed laminar heating distribution on an unadapted grid (Fig. 7b) can be comparable to that of turbulent experimental data (Fig. 3b), which could lead to incorrect conclusions about the state of the wake. Such a preliminary comparison with computational results from a nonoptimized grid was one of the reasons that the experimental data discussed in the present paper were originally thought to result from a laminar wake.[4] The grid structure also should be considered as one of the possible reasons for the disagreement seen in wake-heating comparisons such as those Refs. 10 and 13, although other issues such as flow quality, rarefaction effects, and thermochemical models in the computational fluid dynamics codes also must be considered.

## Conclusions

Experiments and computations have been performed for a 70-deg sphere-cone entry vehicle geometry at Mach 10. The experiments were conducted in a perfect-gas wind tunnel, and a laminar, axisymmetric/two-dimensional Navier–Stokes solver with a perfect-gas thermochemical model was used for the computations. Comparisons were made between measured and predicted heating distributions. On the forebody of the model, agreement to within the experimental uncertainty was achieved. However, in the wake, the experimental heating data began to diverge from the computational results just upstream of the free-shear-layer reattachment point on the sting. Computed peak heating rates on the sting varied with the Reynolds number from 6 to 8% of the forebody stagnation point heating, whereas the peak sting heating from the experiment varied from 8 to 15% of the stagnation point heating. From these comparisons it was theorized that transition to turbulence in the wake occurred in the vicinity of the free-shear-layer reattachment point on the model support sting.

## Acknowledgments

This research was funded under NASA Grants NAGW-1331 and NAG1-1663 to North Carolina State University. The first author performed the research in part as a Graduate Research Assistant, Department of Mechanical and Aerospace Engineering, North Carolina State University.

## References

[1]Bourke, R. D., Golombek, M. P., Spear, A. J., and Sturms, F. M., "MESUR and Its Role in an Evolutionary Mars Exploration Program," 43rd Congress of the International Astronautical Federation, IAF Paper 92-0509, Washington, DC, Aug.–Sept. 1992.

[2]Hollis, B. R., and Perkins, J. N., "High-Enthalpy Aerothermodynamics of a Mars Entry Vehicle, Part 1: Experimental Results," *Journal of Spacecraft and Rockets*, Vol. 34, No. 4, 1997, pp. 449–456.

[3]Hollis, B. R., and Perkins, J. N., "High-Enthalpy Aerothermodynamics of a Mars Entry Vehicle, Part 2: Computational Results," *Journal of Spacecraft and Rockets*, Vol. 34, No. 4, 1997, pp. 457–463.

[4]Hollis, B. R., and Perkins, J. N., "High-Enthalpy and Perfect-Gas Heating Measurements on a Blunt Cone," *Journal of Spacecraft and Rockets*, Vol. 33, No. 5, 1996, pp. 628–635.

[5]Hollis, B. R., "Experimental and Computational Aerothermodynamics of a Mars Entry Vehicle," NASA CR-201633, Dec. 1996.

[6]Horvath, T. J., McGinley, C. B., and Hannemann, K., "Blunt Body Near Wake Flow Field at Mach 6," AIAA Paper 96-1935, June 1996.

[7]Horvath, T. J., and Hannemann, K., "Blunt Body Near Wake Flow Field at Mach 10," AIAA Paper 97-0986, Jan. 1997.

[8]Kastell, D., Horvath, T. J., and Eitelberg, G., "Nonequilibrium Flow Expansion Around a Blunted Cone," *Proceedings of the 2nd European Symposium on Aerothermodynamics*, edited by J. J. Hunt, ESA, Noordwijk, The Netherlands, 1994, pp. 383–389.

[9]Mitchletree, R. A., and Gnoffo, P. A., "Wake Flow About a MESUR Mars Entry Vehicle," AIAA Paper 94-1958, June 1994.

[10]Haas, B. L., and Venkatapathy, E., "Mars Pathfinder Computations Including Base-Heating Predictions," AIAA Paper 95-2086, June 1995.

[11]Gochberg, L. A., Allen, G. A., Gallis, M. A., and Deiwert, G. S., "Comparison of Computations and Experiments for Nonequilibrium Flow Expansions Around a Blunted Cone," AIAA Paper 96-0031, Jan. 1996.

[12]Allegre, J., and Bisch, D., "Blunted Cone at Rarefied Hypersonic Conditions. Experimental Density Flow Fields, Heating Rates and Aerodynamic Forces," Centre National de la Recherche Scientifique, CNRS Rept. RC 95-2, Meudon, France, Sept. 1995.

[13]Holden, M., Kolly, J., and Chadwick, K., "Calibration, Validation and Evaluation Studies in the LENS Facility," AIAA Paper 95-0291, Jan. 1995.

[14]Holden, M., Harvey, J., Boyd, I., George, J., and Horvath, T., "Experimental and Computational Studies of the Flow over a Sting Mounted Planetary Probe," AIAA Paper 97-0768, Jan. 1997.

[15]Moss, J. N., Price, J. M., Dogra, V. K., and Hash, D. B., "Comparison of DSMC and Experimental Results for Hypersonic External Flows," AIAA Paper 95-2028, June 1995.

[16]Micol, J. R., "Hypersonic Aerodynamic/Aerothermodynamic Testing Capabilities at Langley Research Center: Aerothermodynamic Facilities Complex," AIAA Paper 95-2107, June 1995.

[17]Schultz, D. L., and Jones, T. V., "Heat Transfer Measurements in Short-Duration Hypersonic Facilities," AGARD Rept. AG-165, Feb. 1973.

[18]Candler, G. V., and MacCormack, R. W., "Computation of Weakly Ionized Flows in Thermochemical Nonequilibrium," *Journal of Thermophysics and Heat Transfer*, Vol. 5, No. 3, 1991, pp. 226–273.

[19]MacCormack, R. W., and Candler, G. V., "The Solution of the Navier–Stokes Equations Using Gauss–Seidel Line Relaxation," *Computers and Fluids*, Vol. 17, No. 1, 1989, pp. 133–150.

[20]Thompson, J. F., Thames, F. C., and Mastin, C. W., "Automatic Numerical Generation of Body-Fitted Curvilinear Coordinate System for Field Containing any Number of Arbitrary Two-Dimensional Bodies," *Journal of Computational Physics*, Vol. 15, No. 3, 1974, pp. 299–319.

[21]Steger, J. L., and Sorenson, R. L., "Automatic Mesh-Point Clustering Near a Boundary in Grid Generation with Elliptic Partial Differential Equations," *Journal of Computational Physics*, Vol. 33, No. 3, 1979, pp. 405–410.

[22]Gnoffo, P. A., Hartung, L. C., and Greendyke, R. B., "Heating Analysis for a Lunar Transfer Vehicle at Near-Equilibrium Flow Conditions," AIAA Paper 93-0270, Jan. 1993.

[23]Alter, S. J., "The Volume Grid Manipulator (VGM): A Grid Reusability Tool," NASA CR-472, April 1997.

[24]Lees, L., "Hypersonic Wakes and Trails," *AIAA Journal*, Vol. 2, No. 3, 1964, pp. 417–428.

[25]Demetriades, A., "Hot-Wire Measurement in the Hypersonic Wakes of Slender Bodies," *AIAA Journal*, Vol. 2, No. 2, 1964, pp. 245–250.

[26]Zeiberg, S. L., "Transition Correlations for Hypersonic Wakes and Trails," *AIAA Journal*, Vol. 2, No. 3, 1964, pp. 564, 565.

[27]Bird, G. A., *Molecular Gas Dynamics and the Direct Simulation of Gas Flows*, Clarendon, Oxford, 1994, pp. 17–21.

B. A. Bhutta
*Associate Editor*